PHYSICAL REVIEW A **93**, 033402 (2016)

Photoelectron angular distributions in bichromatic atomic ionization induced by circularly polarized VUV femtosecond pulses

Nicolas Douguet,[1] Alexei N. Grum-Grzhimailo,[2] Elena V. Gryzlova,[2] Ekaterina I. Staroselskaya,[3]
Joel Venzke,[1] and Klaus Bartschat[1]
[1]*Department of Physics and Astronomy, Drake University, Des Moines, Iowa 50311, USA*
[2]*Skobeltsyn Institute of Nuclear Physics, Lomonosov Moscow State University, Moscow 119991, Russia*
[3]*Faculty of Physics, Lomonosov Moscow State University, Moscow 119991, Russia*

(Received 10 January 2016; published 2 March 2016)

We investigate two-pathway interferences between nonresonant one-photon and resonant two-photon ionization of atomic hydrogen. In particular, we analyze in detail the photoionization mediated by the fundamental frequency and the second harmonic of a femtosecond VUV pulse when the fundamental is tuned near an intermediate atomic state. Following our recent study [Phys. Rev. A **91**, 063418 (2015)] of such effects with linearly polarized light, we analyze a similar situation with circularly polarized radiation. As a consequence of the richer structure in circularly polarized light, characterized by its right-handed or left-handed helicity, we present and discuss various important features associated with the photoelectron angular distribution.

DOI: 10.1103/PhysRevA.93.033402

I. INTRODUCTION

The control of quantum phenomena represents a crucial challenge, from both experimental and theoretical standpoints. One possible way to achieve "coherent control" at the quantum level [1–3] is to manipulate two-pathway interferences by tuning a parameter that is directly responsible for the interference phenomenon. As a result, the probability for finding the affected quantum system in a definite final state can be varied in a predictable manner.

In two-pathway coherent control of photoionization, one may adopt a scheme in which the photoelectron is emitted from absorption of an odd number of photons through one path and an even number of photons through another path, as for instance in $\omega + 2\omega$ processes. The resulting interference induces noticeable effects only if the two paths have comparable probability amplitudes. The latter condition might be fulfilled by tuning the fundamental frequency near an optically allowed intermediate state, thus enhancing the probability for two-photon absorption. However, the interference phenomenon does not affect the total ionization yield (unless an external electric field is applied [4,5]), but instead manifests itself in the photoelectron angular distribution (PAD) [6–11]. Therefore, the phase difference between two distinct ionizing pathways can, in principle, be used to manipulate the PAD.

The study of two-pathway interferences in photoionization is not limited to the domain of coherent control, but it is also essential in order to model certain experimental conditions. Recent advances in high-harmonic generation (HHG) and x-ray free-electron lasers (XFELs) have enabled experimentalists to reach the extreme ultraviolet (XUV) and x-ray wavelength domain on the femtosecond (fs) and even attosecond (as) time scales. Radiation from XFELs usually carry at least a tiny fraction of the second harmonic, which cannot always be filtered out completely. Hence it is important to understand the effects of two superimposed harmonics [12] in ionization experiments for different light polarizations. An additional promising idea consists in being able to deconvolve the PAD in order to determine the phase difference, or the time delay, between the fundamental and the second harmonic of a VUV pulse. Finally, counterrotating circularly polarized laser fields have recently attracted significant attention, since it was demonstrated that one can generate electron vortices in photoionization by circularly polarized attosecond pulses in helium [13], as well as isolated elliptically polarized attosecond pulses in neon [14].

In a recent study [15], we considered two-pathway interferences induced by linearly polarized light. In this case, a "left-right" asymmetry is created along the direction of the electric field as a result of interference between partial waves with opposite parities. The theoretical treatment involved solving the time-dependent Schrödinger equation (TDSE) numerically using the split-operator algorithm or the matrix iteration method [16,17]. Furthermore, the time-dependent calculations were complemented by predictions obtained from a perturbative formalism at sufficiently low field intensities.

For the present work, we modified our time-dependent code in order to handle light of arbitrary polarization. As a natural next step, we now consider atomic photoionization processes in a circularly polarized bichromatic field, i.e., an electric field of the form

$$\begin{aligned}\mathcal{E}(t) = F(t)[&\cos(\omega t + \phi_1)\hat{\boldsymbol{x}} - \sin(\omega t + \phi_1)\hat{\boldsymbol{y}} \\ &+ \eta\{\cos(2\omega t + \phi_2)\hat{\boldsymbol{x}} + \mathscr{H}\sin(2\omega t + \phi_2)\hat{\boldsymbol{y}}\}],\end{aligned} \qquad (1)$$

with fundamental frequency ω and second harmonic 2ω. The same envelope function $F(t)$ is used for both the fundamental and the second harmonic, while the ratio of the amplitudes is specified by the real parameter η ($\eta > 0$). The corresponding carrier-envelope phases (CEPs) are denoted by ϕ_1 and ϕ_2, respectively. The geometry of the process is shown in Fig. 1. Equation (1) defines the X and Y axes in terms of the electric-field vector direction at $t = 0$. The unit vectors $\hat{\boldsymbol{x}}$ and $\hat{\boldsymbol{y}}$ specify the plane of circular light in which the fundamental is chosen to have negative helicity, whereas the parameter $\mathscr{H} = \pm 1$ indicates the positive or negative helicity of the second harmonic. Consequently, the cases $\mathscr{H} = \pm 1$ correspond to resulting fields for which the harmonics have opposite or equal helicity, respectively. As will be discussed below, the PADs for the cases of both beams left-circularly polarized or both beams

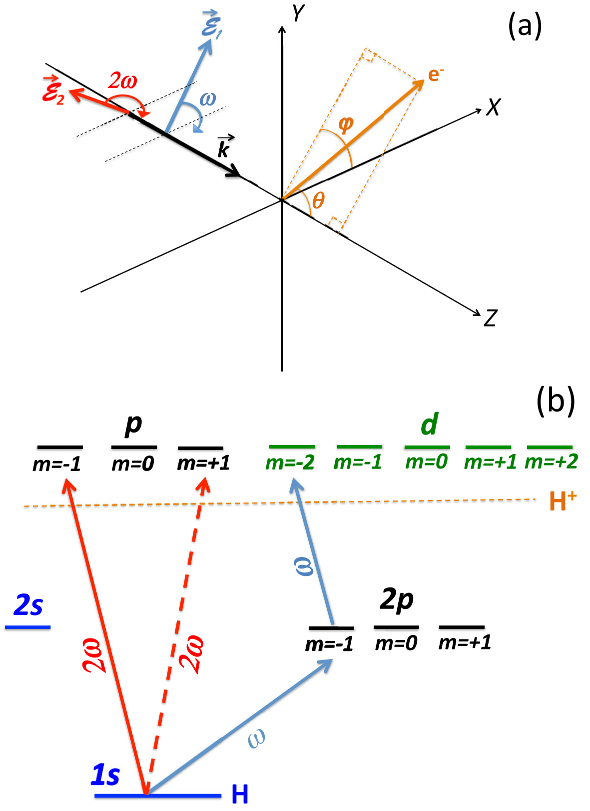

FIG. 1. (a) Bichromatic ionization by left-handed (negative helicity) circularly polarized light propagating along the Z axis. (b) Level scheme of the $\omega + 2\omega$ process. The dashed arrow indicates 2ω ionization with positive light helicity.

right-circularly polarized will be different. The field in Eq. (1) is obtained, with negligible envelope effects for multicycle pulses, from $\boldsymbol{\mathcal{E}}(t) = -c^{-1}\partial\boldsymbol{\mathcal{A}}(t)/\partial t$, with $\boldsymbol{\mathcal{A}}(t)$ denoting the vector potential and c the speed of light. The latter procedure was performed to avoid unphysical pulse-shape effects, as recently discussed in Ref. [18].

For a linearly polarized bichromatic radiation beam, the PAD exhibits an asymmetry with respect to the plane perpendicular to the electric field, while the axial symmetry along the field direction survives. On the other hand, for circularly polarized light the axial symmetry with respect to the light propagation direction, i.e., the Z axis in Fig. 1(a), is broken as a result of interferences, as discussed in detail in [19]. Consequently, circularly polarized light might offer the possibility to manipulate the orientation of the principal direction of photoelectron emission in the XY plane. Additionally, switching from equal to opposite helicity between the two harmonics offers a new degree of freedom to investigate.

The present study shares some similarities with our previous work on linearly polarized light [15]. The asymmetry still occurs as a result of a nonzero time-average cube $\langle\mathcal{E}_x^3\rangle \neq 0$ and $\langle\mathcal{E}_y^3\rangle \neq 0$ of the electric field components, whereas the time average of the field itself vanishes, i.e., $\langle\boldsymbol{\mathcal{E}}\rangle = 0$. We consider again the "multiphoton regime" of ionization for comparatively weak fields (10^{11}–10^{13} W/cm^2) and pulses containing many optical cycles. Stronger fields and shorter pulses may lead to asymmetries already for one-color ionization [20].

Below we investigate in detail the effects of interfering one-photon and two-photon pathways with circularly polarized light, using ionization of atomic hydrogen for the benchmark study and extending our recent results [19]. We concentrate on the photoionization of the hydrogen atom from its $1s$ ground state, using $2p$ as the intermediate state, as shown schematically in Fig. 1(b) for either positive or negative helicity of the second harmonic. We also point out the similarities and differences with the same process for linearly polarized light.

This paper is organized as follows. In Sec. II, we present the theoretical formalism of the PADs for $\omega + 2\omega$ ionization. We also briefly describe the required implementation to compute the solution of the TDSE for circular light polarization, as well as the nonstationary perturbation theory (PT) approach. In Sec. III, we present our numerical results for the hydrogen atom and compare the TDSE with the PT results. We also analyze and discuss the shape of the PADs. The final section is devoted to our conclusions.

Unless indicated otherwise, atomic units (a.u.) are used throughout this manuscript.

II. THEORY

A. Time-dependent Schrödinger equation

Since the general procedure to solve numerically the TDSE was described at length in [21], we only summarize here the necessary modifications to treat circularly polarized light. We consider the propagation of the wave packet with a Hamiltonian $H(\boldsymbol{r},t)$ expressed in the length gauge and the electric dipole approximation as

$$H(\boldsymbol{r},t) = -\frac{\nabla^2}{2} - \frac{1}{r} + \sqrt{\frac{4\pi}{3}}\,r \sum_{q=\pm1} \mathcal{E}_q^*(t) Y_{1q}(\theta,\varphi). \qquad (2)$$

Here we introduced the spherical coordinates (r,θ,φ) of the electron with the Z axis oriented along the light propagation direction [cf. Fig. 1(a)]. The elements $\mathcal{E}_q$, $q = \pm 1$, represent the spherical components of the electric field, expressed in terms of its Cartesian components as $\mathcal{E}_{\pm1} = \mp(\mathcal{E}_x \pm i\mathcal{E}_y)/\sqrt{2}$. When the solution of the TDSE is expanded in partial waves as

$$\Psi(\boldsymbol{r},t) = \frac{1}{r}\sum_{lm} \xi_l^m(r,t) Y_{lm}(\theta,\varphi), \qquad (3)$$

the radial terms $\xi_l^m(r,t)$ are solutions of the following set of coupled equations:

$$i\frac{\partial \xi_l^m(r,t)}{\partial t} = \left[-\frac{1}{2}\frac{\partial^2}{\partial r^2} + \frac{l(l+1)}{2r^2} - \frac{1}{r}\right]\xi_l^m(r,t) + r\sum_{q=\pm1}\sum_{l'm'} \mathcal{E}_q^*(t)\mathcal{I}^{1q}_{lm,l'm'}\xi_{l'}^{m'}(r,t), \qquad (4)$$

with $\mathcal{I}^{k\mu}_{lm,l'm'}$ defined in terms of Clebsch-Gordan coefficients $(l_1m_1,l_2m_2|lm)$ as

$$\mathcal{I}^{k\mu}_{lm,l'm'} = (-1)^{m'}\hat{l}\hat{l}'\hat{k}^{-2}(l0,l'0\,|\,k0)(lm,l'-m'\,|\,k\mu), \qquad (5)$$

where $\hat{a} \equiv \sqrt{2a+1}$. The initial condition is $\xi_l^m(r,0) = \delta_{l0}\delta_{m0}P_{1s}(r)$, where $P_{1s}(r)$ is the ground-state radial orbital of atomic hydrogen. The most general form of the PAD is given by

$$\frac{dW}{d\Omega} = \frac{W_0}{4\pi}\left(1 + \sum_{\substack{k>0\\ 0\leqslant\mu\leqslant k}} |\beta_k^\mu| P_k^\mu(\cos\theta)\cos(\mu\varphi + \psi_k^\mu)\right), \tag{6}$$

where $d\Omega$ is the solid angle corresponding to an electron emitted in the (θ,φ) direction and W_0 is the angle-integrated ionization probability. The anisotropy parameters $\beta_k^\mu = |\beta_k^\mu|\exp(i\psi_k^\mu)$ in Eq. (6), defined for $k > 0$ and $0 \leqslant \mu \leqslant k$, are complex quantities expressed as

$$\beta_k^\mu = N_k^\mu \sum_{lm}\sum_{l'm'} i^{l-l'} e^{i(\sigma_{l'}-\sigma_l)} Z_{El}^{m*} Z_{El'}^{m'} \mathcal{I}_{lm,l'm'}^{k-\mu}. \tag{7}$$

In the above equation, E is the photoelectron energy, $\sigma_l = \arg\Gamma(l+1-i(2E)^{-\frac{1}{2}})$ is the Coulomb phase, and the factor N_k^μ takes the value

$$N_k^\mu = \begin{cases} \hat{k}^2 W_0^{-1} & \text{if } \mu = 0, \\ 2\hat{k}^2\sqrt{\frac{(k-\mu)!}{(k+\mu)!}}\,W_0^{-1} & \text{if } \mu > 0. \end{cases} \tag{8}$$

The partial-wave photoionization amplitudes Z_{El}^m are given by

$$Z_{El}^m = \lim_{t\to\infty}\int_0^\infty P_{El}(r)\xi_l^m(r,t)dr, \tag{9}$$

where $P_{El}(r)$ are energy-normalized Coulomb wave functions. In addition, the angle-integrated ionization probability takes the simple form

$$W_0 = \sum_{lm}|Z_{El}^m|^2. \tag{10}$$

Note that Eqs. (6) and (7) are general and apply to arbitrary light polarization. As an example, the coefficients β_k^0 reduce to the well-known anisotropy parameters for the case of linearly polarized light with electric field vector aligned along the Z axis. Although not explicitly specified in the above equations, β_k^μ, as well as ψ_k^μ, are energy-dependent parameters on the photoelectron line.

In the present treatment of circularly polarized light, the symmetry of the PAD depends on the symmetry character of the various terms entering the sum in Eq. (6). To be more specific, we now turn to the concept of the number of absorbed photons, although when solving the TDSE this concept is not always directly applicable for fields of arbitrary strength. For one-photon ionization alone, only β_2^0 contributes, whereas for two-photon ionization alone, both β_2^0 and β_4^0 contribute. Therefore, in either case, the PADs (6) exhibit even parity π [since $\pi = (-1)^k$], have axial symmetry around the Z axis (due to $\mu = 0$), and are symmetric against reflection with respect to the XY plane (due to $k + \mu =$ even). Considering the case for which both one-photon and two-photon absorption processes are combined, however, contributions from odd k and odd μ, especially β_1^1, β_3^1 (equal helicities), and β_3^3 (opposite helicities), should be accounted for. The latter terms, originating from the interference of amplitudes of the two ionization paths, are responsible for breaking both the inversion and axial symmetries, whereas the reflection symmetry with respect to the XY plane is preserved. The latter symmetry is a consequence of the dipole approximation.

A quantitative description of the axial asymmetry breaking of the PAD can be achieved by introducing a doubly differential angular asymmetry of the form

$$A(\theta,\varphi) = \frac{I(\theta,\varphi) - I(\theta,\pi+\varphi)}{I(\theta,\varphi) + I(\theta,\pi+\varphi)}, \tag{11}$$

where $I(\theta,\varphi) \propto dW/d\Omega$ is the intensity of the electron flux into the solid-angle element $d\Omega$ defined by the angles (θ,φ). In particular, it will be instructive to consider the asymmetry in the XY-polarization plane, i.e., the values of $A(90^\circ,\varphi)$. Further considerations regarding the characterization of the asymmetry for circularly polarized light will be guided by the results of the perturbative approach presented in Sec. II B.

The anisotropy parameters β_k^μ and, therefore, the differential asymmetry (11), are functions of the pulse parameters, i.e., the fundamental frequency, the pulse intensity, the pulse envelope, the second harmonic intensity and helicity, and the CEPs. In this study, we consider pulses of the form (1) covering an integer number N ($N \gg 1$) of optical cycles $T = 2\pi/\omega$, with a pulse envelope $F(t) = F_0\sin^2\Omega t$ ($\Omega = \omega/2N$, $0 \leqslant t \leqslant NT$) and $F(t) = 0$ otherwise. For $N \gg 1$, it can be shown by applying the rotating-wave approximation (RWA) that all significant observables depend only on $\phi = \phi_2 - 2\phi_1$ but not on the individual carrier-envelope phases ϕ_1 or ϕ_2. The latter fact was confirmed numerically for a pulse with $N = 40$ optical cycles, which we used in the TDSE calculations. Therefore, we set $\phi_1 = 0$ below and only vary $\phi = \phi_2$.

Additional details on the method employed to solve the TDSE can be found in [21]. The extension of the code, required to treat light of any polarization in space, is computationally demanding and necessitates the use of parallel architectures, as provided by modern supercomputers like Stampede [22] or SuperMIC [23]. The accuracy of the code in its previous form was tested many times over the years [17,24,25]. The present version was also checked in numerous ways. An important test of accuracy was to reproduce, for linearly polarized light of random orientation in space, earlier results for light polarized along the Z axis.

B. Perturbative approach

In the weak-field regime, the amplitudes can be evaluated within the lowest-order time-dependent perturbation theory. The approach is particularly useful in the case of arbitrarily polarized radiation, in light of the computational complexity associated with solving the TDSE. Furthermore, the PT approach can provide considerable insight by predicting analytically the dependence of physical observables over a wide range of laser parameters. On the other hand, the validity of the PT approach should be tested in order to avoid potential pitfalls in drawing conclusions in an inappropriate parameter regime.

Let us denote by $|El,m\rangle$ the hydrogen eigenstates and by $U_{El,m} \equiv \langle El,m|\hat{U}(NT)|1s\rangle$ the ionization amplitude, with $\hat{U}(t)$ representing the time-evolution operator. In this case, the anisotropy parameters in Eq. (7) can be expressed in terms of

$U_{El,m}$ as

$$\beta_k^\mu = N_k^\mu \sum_{lm} \sum_{l'm'} U^*_{El,m} U_{El',m'} \mathcal{I}^{k-\mu}_{lm,l'm'}, \tag{12}$$

where $\mathcal{I}^{k\mu}_{lm,l'm'}$ is defined by Eq. (5). The ionization amplitudes in Eq. (12) can be evaluated within the lowest-order PT, bearing in mind a number of considerations. As a result of direct photoionization of the $1s$ ground state of hydrogen by the second harmonic of the circularly polarized light, a p photoelectron is emitted, with either positive or negative magnetic quantum number $m = \pm 1$, depending on the field helicity $\mathscr{H} = \pm 1$. On the other hand, only d photoelectrons with $m = -2$ are produced from ionization by the fundamental via a two-photon absorption process with an intermediate real or virtual p state with $m = -1$, as shown in Fig. 1(b). Note a characteristic difference in comparison with the case of linearly polarized light, as no s photoelectron is produced. As a consequence, the resulting interferences are constructed from p and d waves only. In the RWA (which is well satisfied for $N \gg 1$) the only nonvanishing first-order ionization amplitude from the $1s$ state, at a given helicity $\mathscr{H} = \pm 1$, is expressed as

$$\begin{aligned} U^{(1)}_{Ep,\pm 1} &\equiv \langle Ep, \pm 1 \,|\, \hat{U}^{(1)}(NT) \,|\, 1s\rangle \\ &= -i \langle Ep, \pm 1 \,|\, \hat{D} \,|\, 1s\rangle \int_0^{NT} e^{i(E-E_{1s})t'} \mathcal{E}^*_{\pm 1}(t') dt' \\ &= -i D^{(1)}_{Ep} T^{(1)}_{\mathscr{H}=\pm 1}, \end{aligned} \tag{13}$$

whereas the only nonvanishing second-order amplitude is

$$\begin{aligned} U^{(2)}_{Ed,-2} &\equiv \langle Ed, -2 | \hat{U}^{(2)}(NT) | 1s\rangle \\ &= i^2 \sum\!\!\!\!\!\!\!\int_{E_n} \langle Ed, -2 | \hat{D} | E_n p, -1\rangle \langle E_n p, -1 | \hat{D} | 1s\rangle \\ &\quad \times \int_0^{NT} e^{i(E-E_n)t'} \mathcal{E}^*_{-1}(t') \\ &\quad \times \int_0^{t'} e^{i(E_n-E_{1s})t''} \mathcal{E}^*_{-1}(t'') dt'' dt' \\ &= -\sum\!\!\!\!\!\!\!\int_{E_n} D^{(2)}_{Ed}(E_n) T^{(2)}_{E_n}. \end{aligned} \tag{14}$$

The time dependence of the field is contained in the factors $T^{(1)}_{\mathscr{H}=\pm 1}$ and $T^{(2)}_{E_n}$. The radial dipole matrix elements in (13) and (14) are given, respectively, by

$$\begin{aligned} D^{(1)}_{Ep} &\equiv \langle Ep, \pm 1 | \hat{D} | 1s\rangle \\ &= -i\, e^{i\sigma_p} \frac{1}{\sqrt{3}} \int_0^\infty P_{Ep}(r) r P_{1s}(r) dr \end{aligned} \tag{15}$$

and

$$\begin{aligned} D^{(2)}_{Ed}(E_n) &\equiv \langle Ed, -2 | \hat{D} | E_n p, -1\rangle \langle E_n p, -1 | \hat{D} | 1s\rangle \\ &= -e^{i\sigma_d} \sqrt{\frac{2}{15}} \int_0^\infty P_{Ed}(r) r P_{E_n p}(r) dr \\ &\quad \times \int_0^\infty P_{E_n p}(r) r P_{1s}(r) dr. \end{aligned} \tag{16}$$

Here $P_{E_n p}(r)$ denotes the radial orbitals of the intermediate states $|E_n p, -1\rangle$ with energy E_n. The time-dependent factor in Eq. (13) takes the form

$$T^{(1)}_{\mathscr{H}=\pm 1} = \mp e^{-i\phi} \frac{F_0}{\sqrt{2}} \int_0^{NT} \sin^2(\Omega t') e^{-2i\omega t'} e^{i(E-E_{1s})t'} dt'. \tag{17}$$

The ionization amplitude in (13) is thus seen to be proportional to the factor $e^{-i\phi}$. The time-dependent factor of the second-order amplitude (14) is of the form

$$\begin{aligned} T^{(2)}_{E_n} &= \frac{F_0^2}{2} \int_0^{NT} \sin^2(\Omega t') e^{-i\omega t'} e^{i(E-E_n)t'} \\ &\quad \times \int_0^{t'} \sin^2(\Omega t'') e^{-i\omega t''} e^{i(E_n-E_{1s})t''} dt'' dt'. \end{aligned} \tag{18}$$

We now introduce the reduced symbols $\mp U^{(1)}_p \equiv U^{(1)}_{Ep,\pm 1}$ and $U^{(2)}_d \equiv U^{(2)}_{Ed,-2}$ for brevity in the following expressions. The nonvanishing real anisotropy parameters [Eq. (12), μ=0], which are independent of the field helicity, then take the form

$$\beta_2^0 = -W_0^{-1} \left[\eta^2 \left|U^{(1)}_p\right|^2 + \tfrac{10}{7} \left|U^{(2)}_d\right|^2\right], \tag{19}$$

$$\beta_4^0 = \tfrac{3}{7} W_0^{-1} \left|U^{(2)}_d\right|^2. \tag{20}$$

Here the ionization probability is given by

$$W_0 = \left|U^{(2)}_d\right|^2 + \eta^2 \left|U^{(1)}_p\right|^2, \tag{21}$$

and the (dimensionless) probability for ionizing the hydrogen atom during the entire pulse is $\mathscr{P} = \int W_0 dE$. The relation

$$\beta_2^0 + \beta_4^0 = -1 \tag{22}$$

holds, where $-\frac{10}{7} \leqslant \beta_2^0 \leqslant -1$, and $0 \leqslant \beta_4^0 \leqslant \frac{3}{7}$. Considering the case of equal helicities, i.e., $\mathscr{H} = -1$, one obtains two additional nonvanishing complex quantities, β_1^1 and β_3^1, while for opposite helicities ($\mathscr{H} = +1$) one obtains a single additional nonvanishing complex quantity β_3^3. The latter three parameters are proportional:

$$\beta_1^1 = -6\beta_3^1 = 12\beta_3^3 = \frac{6}{\sqrt{5}} \eta W_0^{-1} \left(U^{(2)*}_d U^{(1)}_p\right). \tag{23}$$

Thus the PAD is characterized by only three independent real quantities and Eq. (6) may be presented, for example [19], as

$$\begin{aligned} \frac{dW}{d\Omega} &= \frac{W_0}{4\pi} \Bigg(1 + \sum_{k=2,4} \beta_k^0 P_k(\cos\theta) \\ &\quad + \frac{15}{2} \left|\beta_3^1\right| \sin^3\theta \cos(\mu\varphi + \psi)\Bigg) \\ &= \frac{W_0}{8\pi} \sin^2\theta \Bigg(10 + 7\beta_2^0 - \frac{35}{4}\left(1 + \beta_2^0\right) \sin^2\theta \\ &\quad + 15\left|\beta_3^1\right| \sin\theta \cos(\mu\varphi + \psi)\Bigg). \end{aligned} \tag{24}$$

Here $\mu = \pm 1$ for equal and $\mu = \pm 3$ for opposite helicities, respectively. The upper (lower) sign corresponds to negative (positive) helicity of the fundamental, and

$$\psi = \arg\left(U^{(2)*}_d U^{(1)}_p\right). \tag{25}$$

The PADs determined by Eq. (24) depend on whether both fields have positive or negative helicities. This fact may seem surprising because usually only the relative helicity is important. Since the two frequencies of interest are related by a factor of two, the same configuration of the electric field appears again and again. For example, if both beams are right-circularly polarized, then the maximal field strength $1+\eta$ is achieved at each period in the direction $\varphi_1-\varphi_2$. On the other hand, if both fields are left-circularly polarized, then this direction is characterized by the angle $\varphi_2-\varphi_1$.

The above equations provide an elegant way to characterize the PADs and the asymmetry in both cases of opposite and equal helicities of the fundamental and the second harmonic. It is seen that the PADs (24) possess a perpendicular symmetry plane intersecting the XY plane at angles ψ or $\psi/3$, with respect to the X axis, for equal or opposite helicities, respectively. In addition, the maximum photoelectron emission in each case corresponds to either $\varphi=-\psi$ or $\varphi=-\psi/3$.

In light of these considerations, it is convenient to introduce a *polar asymmetry*, defined along the line of intersection between the plane perpendicular to the radiation beam and the symmetry plane of the PAD. Therefore, the polar asymmetry is given by evaluating the asymmetry in Eq. (11) at either $A(90^\circ,\varphi=-\psi)$ or $A(90^\circ,\varphi=-\psi/3)$, depending on the field helicity. The polar asymmetry in both cases has the same value

$$A=\frac{15}{2}\frac{|\beta_3^1|}{1-\beta_2^0/2+3\beta_4^0/8}=\frac{60|\beta_3^1|}{5-7\beta_2^0}. \tag{26}$$

It is non-negative, i.e., $0\leqslant A\leqslant 1$. After replacing $|\beta_3^1|$ by its real and imaginary parts, $\mathrm{Re}[\beta_3^1]$ and $\mathrm{Im}[\beta_3^1]$, Eq. (26) yields the asymmetry along the X and Y axes, respectively. In contrast to (26), these asymmetries are defined along fixed-in-space directions and, therefore, may change sign.

The polar asymmetry (26) possesses several interesting properties that are worth mentioning. First, the results of Eqs. (19) and (23) indicate that the polar asymmetry depends neither on the field helicity nor on the value of the relative phase ϕ between the second and first harmonic. The validity of this result was checked using both the TDSE and PT methods in the expected domain of validity of perturbation theory. Nevertheless, one might question the appropriateness of Eq. (26) outside the domain of applicability of the PT approach, since the definition of the polar asymmetry itself depends explicitly on the value of ψ, as derived in the PT approach. One should, however, note that the form of the expressions (19)–(26) is in fact more general than might be thought at first sight. Recalling the general expression of the asymmetry parameters (12), considering the RWA, and assuming that the process is dominated by emission of p- and d-electron waves and their interference, the final expressions for the asymmetry parameters β_k^μ and ψ still remain valid to high precision if one substitutes more accurate values of the matrix elements of the time-evolution operator. On the other hand, at large field intensity, when higher-order terms become important, the PAD should differ from expression (24). In particular, the symmetry of the PAD with respect to the plane perpendicular to the XY plane will disappear. In Sec. III, it will be shown that at the largest intensity considered in our study, i.e., 10^{13} W/cm^2, breaking of the symmetry plane remains negligible. Consequently, Eq. (26) still represents an appropriate way to describe the asymmetry.

When evaluating $U_d^{(2)}$ numerically according to Eqs. (14), (16), and (18), we included nine intermediate discrete E_np states ($n=2,3,\ \ldots,10$) in Eq. (14). Further increasing the number of intermediate states to 15 did not change the predicted anisotropy parameters for photon energies in the vicinity of the $1s$-$2p$ transition within the thickness of the lines.

Finally, as in our earlier work [15], we applied perturbation theory with infinitely long "pulses" ($N=\infty$), i.e., continuous radiation of constant amplitude $F_0'=\sqrt{3/8}F_0$. In this case $U_p^{(1)}$ and $U_d^{(2)}$ reduce to

$$U_p^{(1)}=-i\frac{F_0'}{\sqrt{2}}e^{-i\phi}D_{Ep}^{(1)}, \tag{27}$$

$$U_d^{(2)}=i\frac{F_0'^2}{2}\sum_{E_n}\!\!\!\!\!\!\!\int\ \frac{D_{Ed}^{(2)}(E_n)}{E_n-E_{1s}-\omega+i0}. \tag{28}$$

Details of the variationally stable procedure for calculations of the second-order PT amplitude in hydrogen may be found in [26,27].

Equations (19), (20), and (23) can be used to show that, within the model containing the single $2p$ intermediate state and for continuous radiation, the anisotropy parameters take the parametric forms

$$\beta_2^0=-\left(1+\frac{3}{7}\frac{1}{1+\epsilon^2}\right), \tag{29}$$

$$\beta_4^0=\frac{3}{7}\frac{1}{1+\epsilon^2}, \tag{30}$$

$$\beta_1^1=-6\beta_3^1=12\beta_3^3=\frac{C\epsilon}{\epsilon^2+1}. \tag{31}$$

Here

$$\epsilon=\frac{\Delta\omega}{\frac{1}{2}\Gamma_\beta}, \tag{32}$$

$$\Gamma_\beta=\frac{\sqrt{2}F_0'}{\eta}\frac{|D_{E_rd}^{(2)}(E_{2p})|}{|D_{E_rp}^{(1)}|}, \tag{33}$$

$$C=\frac{6i}{\sqrt{5}}e^{i(\sigma_p-\sigma_d-\phi)}, \tag{34}$$

with $\Delta\omega=\omega-(E_{2p}-E_{1s})$. Furthermore, $E_r=2E_{2p}-E_{1s}$ is the photoelectron energy at the resonance ($E_r=0.250$ a.u.). The values of $D_{E_rd}^{(2)}(E_{2p})$ and $D_{E_rp}^{(1)}$ are constants. The lack of the two-photon ionization s channel for circularly polarized radiation makes Eqs. (29) and (30) actually look simpler than the corresponding equations for the anisotropy parameters in the case of linearly polarized radiation [cf. Eqs. (25) and (26) of [15]].

The asymmetry (26) takes the form

$$A=\frac{2|\epsilon'|}{1+\epsilon'^2}, \tag{35}$$

where $\epsilon'=\frac{2}{\sqrt{5}}\epsilon$. Thus the resonance profile of the asymmetry A as function of the photon energy is slightly broader than the profiles of the anisotropy parameters (29)–(31). The widths of

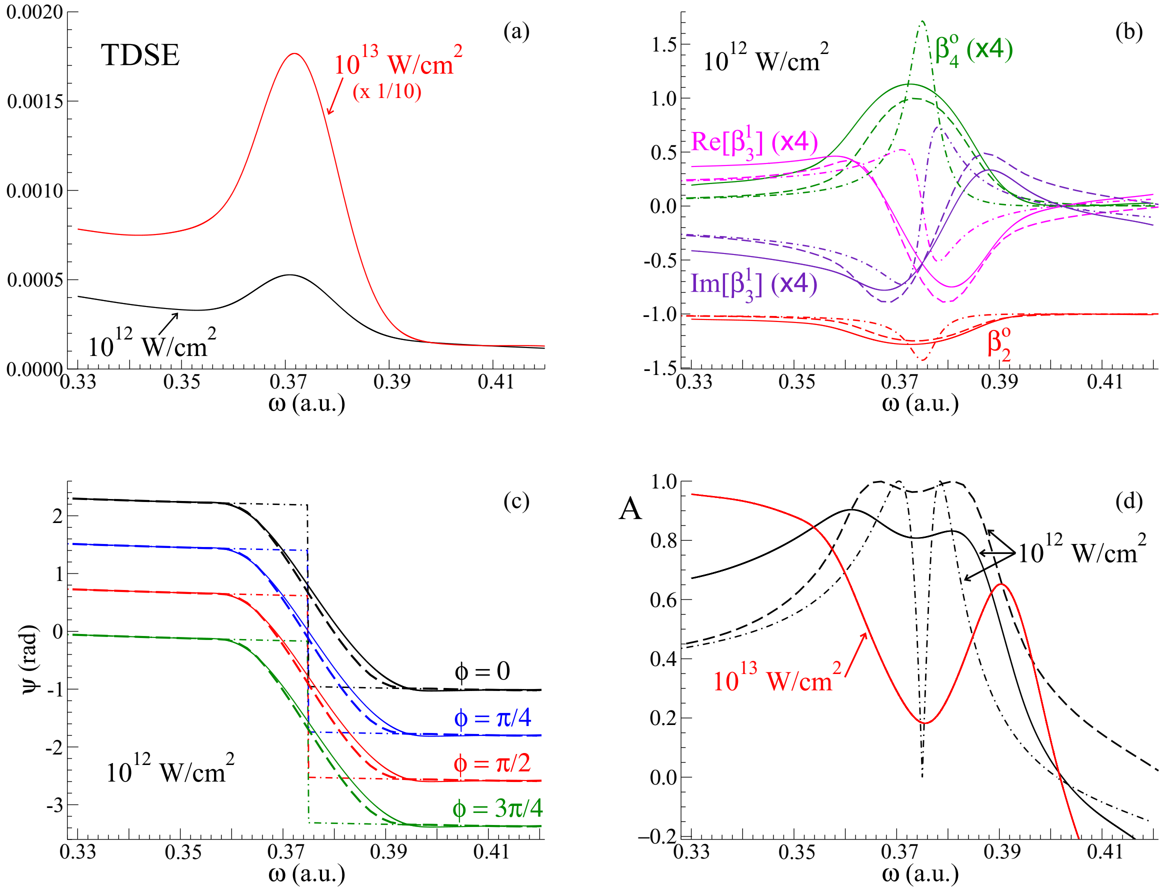

FIG. 2. Results for $\eta = 0.225$. (a) Ionization probability integrated over the main photoelectron line as a function of the photon energy; TDSE ($N = 40$). The other panels show (b) anisotropy parameters β_2^0, β_4^0, and real and imaginary parts of β_3^1 (for $\phi = 0$), averaged over the main photoelectron line, for 10^{12} W/cm^2; (c) angle ψ for 10^{12} W/cm^2 for different relative phases between the harmonics ϕ; (d) polar asymmetry A. In panels (b), (c), and (d): TDSE, $N = 40$ (solid line); PT, $N = 40$ (dashed line); PT, $N = \infty$ (chain line). See text for details.

the resonant structures in the asymmetry and the anisotropy parameters are independent of the relative phase of the harmonics ϕ and also of the interference between the first-order and second-order ionization amplitudes.

The angle ψ defined in (25) undergoes a jump by π when the photon energy crosses the resonance:

$$\psi = \arctan(2\sqrt{2E})^{-1} - \phi + \begin{cases} +\frac{\pi}{2}, & E < E_r, \\ -\frac{\pi}{2}, & E > E_r. \end{cases} \qquad (36)$$

When deriving Eq. (36) we used the recurrence relation for the Coulomb phases (for negative unit charge) [28], $\sigma_{l+1} - \sigma_l = -\arctan[(l+1)\sqrt{2E}]^{-1}$, and the fact that the signs of integrals on the right-hand side of Eqs. (15) and (16) are well defined, and all three are positive.

Although Eqs. (29)–(36) are only valid in a restricted domain of pulse parameters, these analytical results provide a foundation for the qualitative understanding of the features associated with $\omega + 2\omega$ ionization in the vicinity of an intermediate resonance.

III. RESULTS AND DISCUSSION

In order to allow for a direct comparison with our previous study on linearly polarized light [15], we considered a pulse with similar characteristics. Therefore, the calculations were performed for peak intensities spanning a range from 10^{11} W/cm^2 to 10^{13} W/cm^2, with pulse duration corresponding to $N = 40$ cycles of the fundamental frequency, i.e., approximately 6 fs (FWHM of the intensity). As we span different fundamental frequencies while keeping a fixed number of cycles, the pulse durations change slightly, but the effect is not important in our analysis.

We checked the migration of population as a function of time and obtained results similar to $\omega + 2\omega$ ionization by linearly polarized radiation (see the discussion and Fig. 2 in [15]). Thus we expect that the PT approach will be appropriate for 10^{11} W/cm^2, while it would likely fail for 10^{13} W/cm^2.

The ionization probability in the $\omega + 2\omega$ scheme, obtained by solving the TDSE near the $1s$-$2p$ transition frequency, is presented as a function of ω in Fig. 2(a), for intensities of the fundamental of 10^{12} W/cm^2 and 10^{13} W/cm^2, respectively. The curves represent the ionization probability $P = \int P(E)\,dE$, where $P(E)$ is the probability density for ionization yielding a photoelectron with energy E and the integral is taken over the main photoelectron line. The parameter η, which specifies the relative strength of the second harmonic with respect to the fundamental, is chosen to obtain almost equal values of the intensity of the photoelectron line generated by each harmonic separately, thereby allowing for the maximum interference effect. The same value as in Ref. [15], i.e., $\eta = 0.225$, was used, with the associated second-harmonic intensity corresponding to 5% of the fundamental intensity. Although the frequency dependencies depicted in Fig. 2(a) appear similar to the linearly polarized case [15], the ionization probability can differ by more than 20% at some frequencies. The value of the ionization probability confirms the fact that the PT approach is not adequate for $10^{13}\ \mathrm{W/cm^2}$. When increasing the intensity by a factor of 10, second-order PT for two-photon absorption predicts an ionization probability 100 times larger, thus overestimating the TDSE results by approximately a factor of three.

Generally, due to issues related to the experimental resolution, only an averaged value of the anisotropy parameters over the photoelectron line can be measured. For this reason, we actually calculate $\beta_k^\mu = P^{-1}\int \beta_k^\mu(E)P(E)dE$ and will present results for such averaged quantities below. In Fig. 2(b), we plot β_2^0, β_4^0, and β_3^1 calculated in the TDSE and PT approaches, as a function of the fundamental frequency, for $10^{12}\ \mathrm{W/cm^2}$. We only present results for the two negative helicities, since the results for opposite helicities are either the same (for the asymmetry A) or can be deduced by a rescaling factor (for the anisotropy parameters β), as indicated in Eq. (23). The TDSE and the PT results for $N = 40$ are close, showing the applicability of the PT approach. The relation (22), derived in the PT, is still seen in the TDSE results with high accuracy. The resonance profiles of the anisotropy parameters for $N = 40$ are broadened in comparison with the profiles for the continuous radiation due to the spectral width of the pulse. According to Eq. (31), for continuous radiation in the single-resonance approximation, both $\mathrm{Re}[\beta_3^1]$ and $\mathrm{Im}[\beta_3^1]$, which represent the interference effects, change sign at the resonance position. Applying shorter pulses and allowing for other intermediate states leads to separation of the zeros in the real and imaginary parts of the asymmetry parameters (31). This splitting is clearly seen in Fig. 2(b).

As discussed above, the polar asymmetry (26) is defined with respect to the direction that makes an angle ψ with the X axis in the XY plane. This is the line of intersection of the symmetry plane of the PAD with the XY plane. Calculations of the angle ψ with both the TDSE and PT approaches are exhibited in Fig. 2(c) for different relative phases ϕ between the harmonics. The symmetry plane, and therefore the PADs, rotate rapidly near the resonance. The frequency dependence of the angle ψ [Fig. 2(c)] closely follows Eq. (36), except that the jump by π is smoothed out due to the finite duration of the pulse in the case $N = 40$. In the limit of continuous radiation, this rotation is "infinitely fast" at the resonance energy. It actually means dropping the polar asymmetry to zero [Fig. 2(d)] and simultaneously changing the direction of the symmetry axis to the opposite.

In Fig. 2(d) we observe relatively good agreement between the PT and TDSE predictions for $10^{12}\ \mathrm{W/cm^2}$. The polar asymmetry is large in the vicinity of the resonance and drops significantly at higher frequencies. The characteristic energy dependence of the asymmetry near the resonance energy with the local minimum is explained by Eq. (35). In the TDSE and PT calculations for $N = 40$ this expression is convoluted with the frequency spectrum of the pulse. For the longer pulse the local minimum would be deeper, reaching zero in the limit of continuous radiation, as discussed above. Although the polar asymmetry is defined as a non-negative number, A in Fig. 2(d) crosses zero in the high-energy wing of the resonance. We permitted this in the interest of better visibility, and hence we do not show the jump of ψ by $+\pi$ in Fig. 2(c) at the corresponding energies either. In our case the polar asymmetry A crosses zero when $U_d = 0$. Within the PT, the vanishing of the two-photon amplitude out of the resonance is a result of mutual compensation of contributions from the lower-lying $2p$ intermediate state and higher lying intermediate p states, including the p continuum. Therefore, the position of this zero is highly sensitive to the inclusion of the latter continuum [29].

The asymmetries along the X and Y axes (not shown), described by the real and imaginary parts of β_3^1, change sign rapidly near the resonance, as follows from the curves for $\mathrm{Re}[\beta_3^1]$ and $\mathrm{Im}[\beta_3^1]$ in Fig. 2(b). Hence the individual asymmetries along each axial direction behave similarly to the ones for linearly polarized light [15].

The polar asymmetry for $10^{13}\ \mathrm{W/cm^2}$ [Fig. 2(d)] reveals a somewhat erratic and more surprising behavior. It exhibits a deep minimum at the resonance, a sharp local maximum at $\omega = 0.39$ a.u., and is becoming largest at lower frequencies. Note, however, that the maximum at $\omega = 0.39$ a.u. and the largest absolute values at lower frequencies were also predicted for the linearly polarized light for $10^{13}\ \mathrm{W/cm^2}$ [15], thus showing consistency of the results. Although the validity of the polar asymmetry framework may be questionable for $10^{13}\ \mathrm{W/cm^2}$, we will show that three-dimensional representations of the PAD corroborate the relevance of the polar asymmetry, even at such high intensity.

Another aspect to consider is the behavior of the PAD as a function of the relative phase between the two harmonics. Experimentally, such a relative phase can, for instance, be created by introducing a time-delay τ between the two harmonics. For simplicity, let as assume that the first harmonic is of the form $\cos(\omega t + \phi_1)$, with $0^\circ \leqslant \phi_1 \leqslant 360^\circ$ as a randomly distributed carrier-envelope phase (CEP). If we further assume that a time delay τ has been introduced, the second harmonic is described by the nonlinear term $\cos^2(\omega t + \phi_1)$, leading to the form $\cos(2\omega t + \phi_2)$, with $\phi_2 = 2\omega\tau + 2\phi_1$. Using the PT formalism and the RWA, we see from Eqs. (13), (14), (17), and (18) that in the general case $U_p^{(1)} \propto e^{-\phi_2}$ and $U_d^{(2)} \propto e^{-2\phi_1}$. As a result, the interference terms in Eqs. (23) and (25) depend on $2\phi_1 - \phi_2 = -2\omega\tau$, which plays the role of the relative phase ϕ. If the time-delay τ varies randomly, the interference effect would cancel out on average. On the other hand, if τ is locked at some specific value, one can efficiently control the interference terms. For more details, see [30] and references therein.

Figure 3 depicts the behavior of some of the quantities discussed above as a function of the relative phase between the harmonics ϕ at the resonance frequency. We do not show the results of the PT calculations in this figure, because they are very close to the TDSE results. The even-rank anisotropy parameters β_2^0 and β_4^0 keep a constant value, since they are not involved in the $\omega + 2\omega$ interference effects. In addition, the polar asymmetry also remains constant. This is a somewhat unexpected result since the left-right asymmetry for linearly polarized light oscillates as a function of the relative

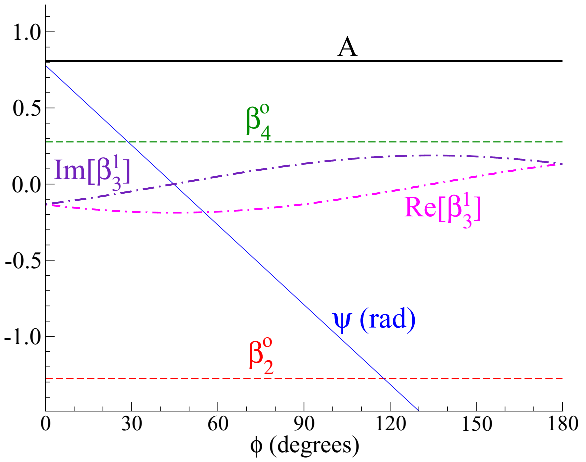

FIG. 3. TDSE results for equal helicities for the anisotropy parameters β_2^0 (dashed red line), β_4^0 (dashed green line), $\mathrm{Re}[\beta_3^1]$ (chain magenta line), and $\mathrm{Im}[\beta_3^1]$ (chain indigo line), as well as the polar asymmetry A (black thick line) and its corresponding symmetry angle ψ (thin blue line). The photon energy is in resonance with the $1s$-$2p$ excitation, the peak intensity is 10^{12} W/cm^2, and $N = 40$. See text for details.

phase between harmonics (see, for example, [7,8,10,15]). The result can be understood, however, by recalling that the polar asymmetry A is defined with respect to a direction that, itself, rotates with the angle ϕ. As mentioned above, it is defined by the absolute values of the anisotropy parameters, independent of ϕ. The angle ψ, which characterizes this direction and the orientation of the symmetry plane of the PAD, is a linear function of the relative phase, $\psi(\phi) = \psi(0^\circ) - \phi$, as expected from Eq. (17). At the same time, the real and imaginary parts of β_3^1 oscillate as functions of ϕ, as shown in Fig. 3.

Although the polar asymmetry and its associated angle ψ provide a quantitative description of the asymmetry generated by interfering one-photon and two-photon pathways with circularly polarized light, they only contain limited information on the PAD. For this reason, it is desirable to directly visualize the three-dimensional PAD [19]. Figure 4 exhibits the PADs for 10^{12} W/cm^2 and $\phi = 0$ for different fundamental frequencies, i.e., on the left and right wing of the resonance ($\omega = 0.330$ a.u. and 0.410 a.u.), and at the resonance energy ($\omega = 0.375$ a.u.). In addition, the PADs are shown for equal (upper panels) and opposite (lower panels) helicities. As anticipated from the values of the asymmetry parameters in Fig. 2, valid for both cases $\mathscr{H} = \pm 1$, the asymmetry of the 3D PADs is large on the left wing [panels (a) and (d)] and almost vanishes, resembling a donut-like shape, on the right wing [panels (c) and (f)] of the resonance. Since the TDSE and PT results are in very good agreement, only the TDSE results are shown here. The maximum asymmetry is observed near the resonance. It is combined with a rapid rotation of the PADs by approximately 90° from $\omega = 0.330$ a.u. to 0.375 a.u. and by 180° when scanning from the left to the right wing of the resonance. This result is in agreement with Eq. (36) and the computed values of ψ in Fig. 2(c).

Figure 5 exhibits the PADs at the largest intensity studied in this work, 10^{13} W/cm^2. The shapes of the PADs confirm that the latter still effectively possess a symmetry plane. The survival of this symmetry plane was discussed above. It is explained by the fact that, even at this large laser intensity, the photoelectron line is still dominated by p- and d-wave emission. We see that the asymmetry of the PAD is small at the resonance, as predicted from the computed polar asymmetry

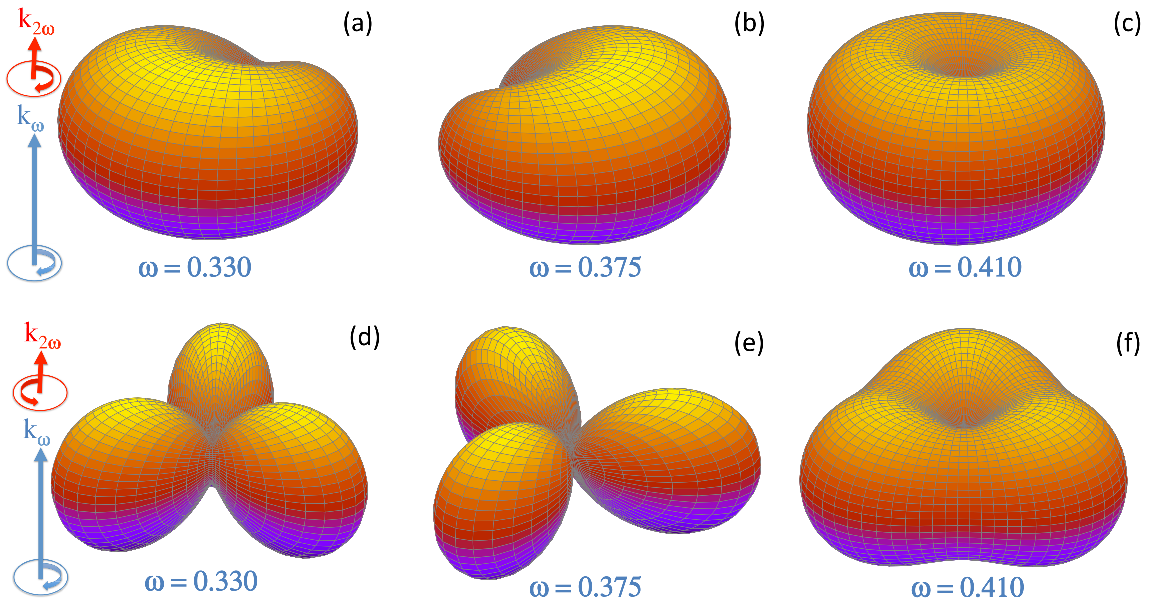

FIG. 4. Three-dimensional PADs calculated in the TDSE approach for 10^{12} W/cm^2, $N = 40$, and relative phase $\phi = 0$. The PADs have been averaged over the photoelectron line and rescaled to improve visualization. Calculations for equal helicities are shown in panels (a), (b), and (c), while results for opposite helicities are depicted in panels (d), (e), and (f). The fundamental frequency is given in atomic units.

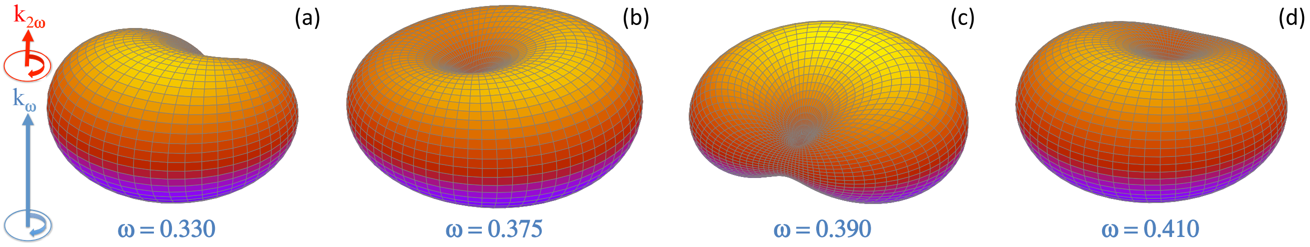

FIG. 5. Same as the upper row in Fig. 4 for 10^{13} W/cm^2.

[cf. Fig. 2(d)]. We also plotted the PAD at the predicted local maximum of the polar asymmetry ($\omega = 0.390$ a.u.).

Figure 6 demonstrates how the asymmetry A and the associated angle ψ evolve with the pulse duration in the vicinity of the $1s$-$2p$ resonance. These 3D plots were generated from the PT predictions, which should be a very good approximation to the TDSE results but are computationally much easier to obtain. For long ($N \sim 1000$) pulses, A and ψ behave as predicted by Eqs. (35) and (36), respectively, for continuous radiation. Small deviations from the symmetric shape prescribed by Eq. (35) are caused by contributions from additional intermediate states np ($n > 2$) and small variations of the radial amplitudes (15) and (16) within the narrow interval of photon frequencies. When the pulse duration is decreased and, correspondingly, the spectral width of the pulse is increased, the sharp resonance-like structure in A is smeared out. This leads to a single broad maximum for $N \sim 10$, but at $N = 40$ a local minimum is still visible [see Fig. 2(d)]. Similarly, the sharp jump in ψ for $N \sim 1000$ transforms into a shallow variation for $N \sim 10$. For the short pulses, the influence of the neighboring $3p$ resonance can explicitly be seen in the high-energy wing of the $2p$ resonance structure.

Another interesting point concerns the determination of the phase ϕ between the harmonics of the XFEL, based on measurements of the PADs. This can be discussed within the domain of applicability of the PT for infinite pulses, where analytical expressions can be developed much further than in the more elaborate computational approaches. A recipe suggested in our recent paper [15] with the use of only linearly polarized radiation is, unfortunately, not valid [31]. The relation between the phase offsets, Eq. (40) in the above paper, is incorrect. Furthermore, since the pulse parameters of XFELs are usually not known precisely, the observed quantities to extract the relative phase of the harmonics should not be very sensitive to these parameters. With circularly polarized light, the angle ψ [Figs. 2(c) and 6(b)] is, in this respect, a good candidate. It is defined by Eq. (36) and can be used in cases where the atomic wave functions are not known in analytic form. In the latter case the scattering phase difference $\sigma_d - \sigma_p$ can be accurately calculated (for example, for He) far from the autoionizing resonances, providing finally the value of ϕ from measurements of the angle ψ.

IV. SUMMARY AND OUTLOOK

Extending previous studies for linearly polarized radiation, we have presented a detailed investigation of two-pathway interferences between nonresonant one-photon and resonant two-photon ionization of atomic hydrogen by circularly polarized photons. General formulas for arbitrary light polarizations were derived and specified for circularly polarized radiation beams. The validity of the predictions based on perturbation theory was analyzed by comparing those predictions with

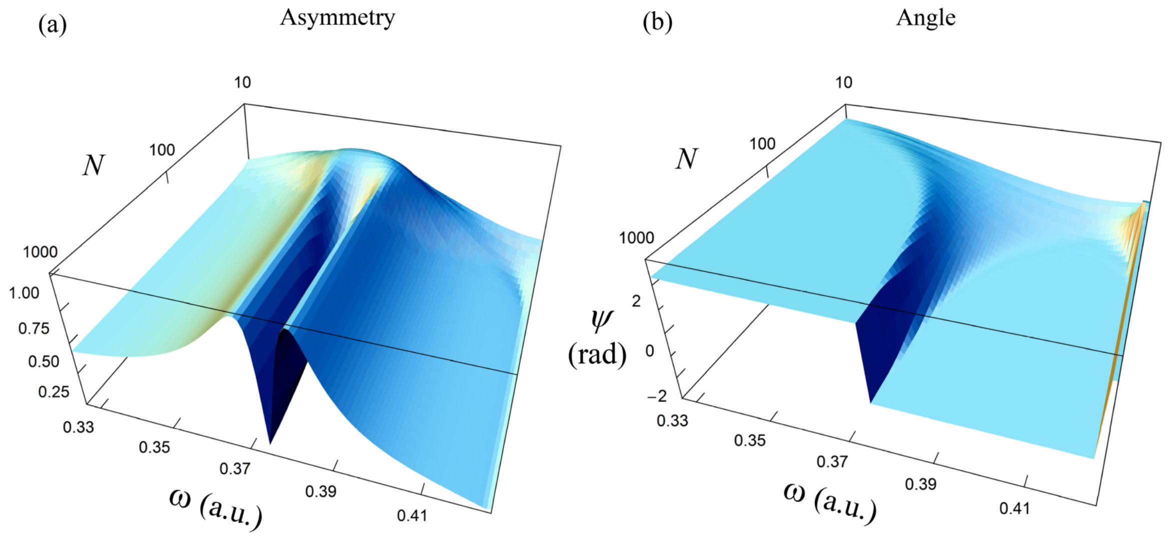

FIG. 6. Polar asymmetry A (a) and associated angle ψ (b) as functions of the energy of the first harmonic and pulse duration (expressed in the number of optical cycles N), calculated in PT for the peak intensity 10^{12} W/cm^2.

results obtained by solving numerically the time-dependent Schrödinger equation.

Allowing for more general polarizations opens up a rich field of further investigations. This was demonstrated with predictions for coherent control of the photoelectron angular distribution that would be achievable by employing circularly polarized radiation fields with equal or opposite helicities. An angle defining the symmetry plane of the PAD and the polar asymmetry of the angular distribution with respect to a variable direction were introduced. Although expressions for these quantities in terms of the channel amplitudes were derived within the perturbation theory, the concepts of the symmetry plane and the polar symmetry keep their meaning far beyond the domain of applicability of the perturbation theory. Finally, analytical dependencies of the parameters that determine the PAD were derived in the vicinity of an isolated intermediate resonance within perturbation theory for continuous radiation as functions of energy.

Given the experimental challenges associated with the preparation of atomic hydrogen targets, it is likely that such experiments would first be performed for systems that are more convenient from a practical point of view. Targets that come to mind are the light noble gases, such as helium, neon, and possibly argon. In fact, initial experiments on helium and neon were recently performed at the FERMI free-electron laser facility in Trieste (Italy) [30,32]. Several more studies are planned within the upcoming months [33]. While the current experimental laser parameters, namely relatively long and strong pulses, as well as experimental details such as the pulse form varying from shot to shot and the need for focal averaging over the interaction region, will make a *quantitative* comparison between experiment and theory virtually impossible at the present time, it has already become evident that studies like the present one are essential to *qualitatively* predict possibly interesting effects and thereby help in the planning of such highly sophisticated and very expensive experimental endeavors.

ACKNOWLEDGMENTS

The authors benefited greatly from stimulating discussions with Giuseppe Sansone, Kevin Prince, and Kiyoshi Ueda. The work of N.D., J.V., and K.B. was supported by the United States National Science Foundation under Grant No. PHY-1430245 and the XSEDE allocation No. PHY-090031. The calculations were performed on Stampede at the Texas Advanced Computing Center in Austin and SuperMIC at the Center for Computation & Technology at Louisiana State University in Baton Rouge.

[1] M. Shapiro and P. Brumer, J. Chem. Phys. **84**, 4103 (1986).
[2] P. Brumer and M. Shapiro, *Principles of the Quantum Control of Molecular Processes* (Wiley-VCH, Berlin, 2003).
[3] C. Brif, R. Chakrabati, and H. Rabitz, New J. Phys. **12**, 075008 (2010).
[4] N. L. Manakov, V. D. Ovsiannikov, and A. F. Starace, Phys. Rev. Lett. **82**, 4791 (1999).
[5] A. Bolovinos, S. Cohen, and I. Liontos, Phys. Rev. A **77**, 023413 (2008).
[6] K. J. Schafer and K. C. Kulander, Phys. Rev. A **45**, 8026 (1992).
[7] N. B. Baranova, I. M. Beterov, B. Ya. Zel'dovich, I. I. Ryabtsev, A. N. Chudinov, and A. A. Shul'ginov, Pis'ma Zh. Eksp. Teor. Fiz. **55**, 431 (1992) [JETP Lett. **55**, 439 (1992)].
[8] Y.-Y. Yin, C. Chen, D. S. Elliott, and A. V. Smith, Phys. Rev. Lett. **69**, 2353 (1992).
[9] Z.-M. Wang and D. S. Elliott, Phys. Rev. Lett. **87**, 173001 (2001).
[10] R. Yamazaki and D. S. Elliott, Phys. Rev. Lett. **98**, 053001 (2007).
[11] R. Yamazaki and D. S. Elliott, Phys. Rev. A **76**, 053401 (2007).
[12] L. A. A. Nikolopoulos and P. Lambropoulos, Phys. Rev. A **74**, 063410 (2006).
[13] J. M. Ngoko Djiokap, S. X. Hu, L. B. Madsen, N. L. Manakov, A. V. Meremianin, and A. F. Starace, Phys. Rev. Lett. **115**, 113004 (2015).
[14] L. Medišauskas, J. Wragg, H. van der Hart, and M. Yu. Ivanov, Phys. Rev. Lett. **115**, 153001 (2015).
[15] A. N. Grum-Grzhimailo, E. V. Gryzlova, E. I. Staroselskaya, J. Venzke, and K. Bartschat, Phys. Rev. A **91**, 063418 (2015).
[16] M. Nurhuda and F. H. M. Faisal, Phys. Rev. A **60**, 3125 (1999).
[17] A. N. Grum-Grzhimailo, B. Abeln, K. Bartschat, D. Weflen, and T. Urness, Phys. Rev. A **81**, 043408 (2010).
[18] K. Bartschat, J. Venzke, and A. N. Grum-Grzhimailo, Phys. Rev. A **91**, 053404 (2015).
[19] A. N. Grum-Grzhimailo, E. V. Gryzlova, E. I. Staroselskaya, S. I. Strakhova, J. Venzke, N. Douguet, and K. Bartschat, J. Phys.: Conf. Ser. **635**, 012008 (2015).
[20] L.-Y. Peng and A. F. Starace, Phys. Rev. A **76**, 043401 (2007).
[21] A. N. Grum-Grzhimailo, A. D. Kondorskiy, and K. Bartschat, J. Phys. B **39**, 4659 (2006).
[22] https://www.tacc.utexas.edu/stampede/.
[23] http://www.hpc.lsu.edu/resources/hpc/system.php?system=SuperMIC.
[24] A. N. Grum-Grzhimailo, M. N. Khaerdinov, and K. Bartschat, Phys. Rev. A **88**, 055401 (2013).
[25] I. A. Ivanov, A. S. Kheifets, K. Bartschat, J. Emmons, S. M. Buczek, E. V. Gryzlova, and A. N. Grum-Grzhimailo, Phys. Rev. A **90**, 043401 (2014).
[26] B. Gao and A. F. Starace, Phys. Rev. A **39**, 4550 (1989).
[27] E. I. Staroselskaya and A. N. Grum-Grzhimailo, Vest. Mosk. Univ. Fiz. **N5**, 45 (2015) [Moscow Univ. Phys. Bull. **70**, 374 (2015)].
[28] *Handbook of Mathematical Functions With Formulas, Graphs, and Mathematical Tables*, edited by M. Abramowitz and I. A. Stegun (Dover Publications, New York, 1964).
[29] A. T. Georges and P. Lambropoulos, in *Advances in Electronics and Electron Physics*, edited by L. Marton and C. Marton (Academic Press, New York, 1980), Vol. 54, p. 191.
[30] K. C. Prince *et al.*, Nat. Photon. **10**, 176 (2016).
[31] A. N. Grum-Grzhimailo, E. V. Gryzlova, E. I. Staroselskaya, J. Venzke, and K. Bartschat, Phys. Rev. A **93**, 019901 (2016).
[32] https://www.elettra.trieste.it/FERMI/.
[33] G. Sansone and K. C. Prince (private communication).